https://doi.org/10.56801/MME1029

Numerical Simulation for Cooling of Integrated Toroidal Octagonal Inductor Using Nanofluid in a Microchannel Heat Sink

Yamina Benhadda[1*], Mokhtaria Derkaoui[2], Hayet Kharbouch[1], Azzeddine Hamid[3], Pierre Spiteri[4]

[1]*LEPA Laboratory, Faculty of Electrical Engineering, University of Science and Technology, Mohammed Boudiaf USTOMB, Oran, Algeria*
[2]*LEPA Laboratory, National Institute of Telecommunications & ICT, Oran, Algeria*
[3]*Center Nour Bachir, El Bayadh, Algeria*
[4]*INP-ENSEEIHT, IRIT, Toulouse, France*
[*]*Email: yamina.benhadda@univ-usto.dz*

Received: 17-11-2023
Accepted: 06-12-2023

Abstract: This paper presents a comprehensive numerical simulation study focused on the cooling of integrated toroidal octagonal inductor using nanofluids within a microchannel heat sink. The investigation utilizes COMSOL Multiphysics 6.0 integrated with the Fluid Flow and Conjugate Heat Transfer Module. The primary objective is to explore and understand fluid flow and heat transfer characteristics within the integrated inductor. The study involves testing three distinct fluids, water, CuO-water nanofluid, and Al_2O_3-water nanofluid, under laminar flow conditions within microchannels. The choice of fluid plays a significant role in heat transfer, interacting with the microchannel geometry to optimize performance. Three-dimensional computational fluid dynamics (CFD) models are meticulously developed; focusing on toroidal inductors equipped with micro pin fins heat sinks. The study commences by detailing the geometry of the micro coil and the integrated heat sink. The simulation encompasses a mathematical model that captures the intricate interplay between the governing Navier-Stokes equations for fluid dynamics and the heat transfer equations within the integrated inductor. As φ increases, temperature, viscosity, and pressure decrease. CuO-water and Al_2O_3-water nanofluids play a significant role in influencing laminar flow and key thermal parameters in the toroidal inductor. These nanofluids, which consist of base fluids (water) with dispersed nanoparticles (CuO or Al_2O_3), are employed as cooling agents to enhance heat transfer. The presence of nanoparticles in the fluid alters its thermal properties, leading to changes in the flow dynamics and overall heat dissipation within the toroidal inductor.

The laminar flow characteristics are affected by the nanofluid's viscosity, density, and thermal conductivity. Additionally, the Nusselt number, Reynolds number, and thermal resistance are key thermal parameters that reflect the performance of the cooling system. The nanofluid's influence on these parameters is crucial for understanding and optimizing the thermal management of the integrated toroidal inductor.

The enhancement of heat dissipation in the toroidal inductor is achieved through improved thermal properties of the nanofluid. Higher nanoparticle concentrations result in better heat transfer rates, leading to lower temperatures in the toroidal inductor. This, in turn, improves the overall efficiency and performance of the cooling system. The viscosity of the nanofluid is influenced by the presence of nanoparticles. The pressure within the microchannels is also affected by the nanoparticle concentration. An increase in φ can lead to changes in pressure drop along the microchannels. Understanding these variations is crucial for designing an effective cooling system.

Keywords: Cooling, integrated toroidal octagonal inductor, Nanofluid, Heat sink, microchannels, CuO/water, Al_2O_3/water.

1. Introduction

Rapid advances in micro-electro mechanical systems (MEMS) have inspired extensive research into the development of innovative micro-cooling technologies. A variety of methods have been studied, including micro-jet impact, micro-heat pipes, micro-electro-hydrodynamic systems, and microchannel heat sink. As electronic components become smaller in size and the performance of integrated inductors improves, the heat flow generated increases significantly. This phenomenon poses a huge challenge to traditional thermal management solutions, and microchannels heat sink has attracted widespread attention in recent years due to their superior heat dissipation capabilities and minimal hydraulic losses. There are many studies in the literature dealing with various aspects of using microchannels heat sink for heat transfer applications. Traditional microchannels have elongated microchannels parallel to the base [1]. Analytical and numerical models have been proposed to predict heat transfer through these heat sinks [2-4]. Herries et al. [5] studied the flow and heat transfer characteristics of various nanofluids (ZnO-water, Al_2O_3-water, SiO_2-water, CuO-water) in hexagonal microchannel heat sinks. In particular, Al_2O_3-water nanofluid showed excellent heat transfer performance, while CuO-water nanofluid showed lower pressure drop. Li and Peterson [6] experimentally studied the effects of temperature and volume fraction on the effective thermal conductivity of nanofluids, showing that the thermal conductivity of certain nanofluid compositions significantly increased. Mirzai et al. [7] performed a numerical study on the heat transfer and friction coefficients in microchannels filled with Al_2O_3-water nanofluids, and the results showed that the friction coefficients and heat transfer coefficients increased compared to pure water. Khoshvaght-Aliabadi [8] performed a numerical study of forced convection in a sinusoidal channel. The effects of channel height and wave amplitude on Nusselt number and friction coefficient are revealed, and relevant prediction suggestions are put forward. These parameters are valid for water and Al_2O_3-water nanofluids. Farzad Pourfattah et al. [9] aimed to numerically simulate heat transfer and fluid flow characteristics of CuO-water nanofluid under a laminar flow regime in a manifold microchannel. Their study highlighted the substantial enhancement of heat transfer attributed to nanoparticles, surpassing the effects of pressure drop. Van Erp et al. [10] developed an innovative approach by etching microchannels directly under the silicon substrate of the chip. This design allowed for the direct contact of the chip's hot spot with the internal microchannel, effectively reducing thermal resistance in the heat sink. J. Cheng et al. [11] tackled the optimization of flow and heat transfer performance of a manifold microchannel heat sink. Their innovative design incorporated a water surface wave structure and incorporated micro-jet impingement with CuO-water nanofluid as the coolant.

In the context of these developments, this paper aims to perform numerical simulations of laminar flow and heat transfer in an inductor cooled by a heat sink equipped with microchannels. The importance of heat sink applications in integrated inductors and the rarity of cooling systems in such configurations triggered the investigation of this study. The unique geometry of toroidal inductors [12-16] presents modeling challenges and often requires closed-form equations or fabrication/electromagnetic (EM) modeling.

The novel toroidal design offers a simplified approach while maintaining improved performance, making them critical to the advancement of industry and research. Obviously, fluids with higher thermal properties must be circulated.

This article focuses on water-cooled integrated toroidal inductor and compares this to metallic liquids composed of nanoparticles such as copper oxide CuO or aluminum oxide Al_2O_3. The resulting nanofluids CuO-water and Al_2O_3-water exhibited improved thermal properties and increased heat transfer capacity compared to pure water. The study begins by describing the study area and discussing the microcoil geometry and dimensions. The structure and performance of microchannel heat sinks are also described in detail. A mathematical model is built to simulate the complex coupling between the Navier-Stokes equations governing fluid dynamics and the heat transfer equations within integrated inductor. A computational 3D fluid dynamics model of an inductor equipped with a heat sink was created, including laminar flow and heat transfer modules, and the model was numerically solved using the finite element method supported by Comsol Multiphysics 6.0.

The need for circulating a fluid with higher thermal properties is apparent. This paper focuses on cooling the integrated toroidal octagonal inductor using water and compares it with a metallic fluid composed of nanoparticles such as copper oxide (CuO) or aluminum oxide (Al_2O_3). The resulting nanofluids, CuO-water and Al_2O_3-water, exhibit improved thermal attributes and enhanced heat transfer capacity compared to pure water.

The study commences with a description of the study domain, elaborating on the micro coil's geometry and dimensions. The microchannel heat sink's structure and properties are also detailed. A mathematical model is developed to simulate the intricate coupling between the Navier-Stokes equations governing fluid dynamics and the heat transfer equations within the integrated inductor.

Three-dimensional computational fluid dynamics (CFD) models of the toroidal inductor equipped with the heat sink are established, encompassing laminar flow and heat transfer modules. The finite element method, facilitated by Comsol Multiphysics 6.0, is employed to numerically solve the model.

A comprehensive exploration of heat transfer and fluid flow in the integrated toroidal inductor is presented. The ensuing sections discuss the numerical findings, including the impact of heat sink integration, and the influence of nanofluid volume fraction. The study's parameters, such as temperature, velocity, pressure, Reynolds number, Nusselt number, and thermal resistance are fully parameterized for ease of extension and exploration.

2. Numerical Simulation

The numerical simulation of cooling of integrated toroidal octagonal inductor using nanofluids and microchannel heat sink is conducted under a set of well-defined assumptions to accurately model the heat transfer and fluid dynamics. The study assumes steady-state conditions, involving an incompressible fluid with laminar flow characteristics. The properties of both the fluids and solid materials are considered to remain constant throughout the simulation. Moreover, the effects of viscous dissipation are considered negligible, allowing the focus to remain on the primary mechanisms of heat transfer. The simulation considers a constant temperature at the inlet and a constant heat flux applied at the bottom of the system. Additionally, a pressure of zero is assumed at the outlet. These assumptions collectively provide

a structured foundation for investigating the cooling behavior of the integrated toroidal octagonal inductor using nanofluids and a microchannel heat sink. By employing these assumptions, the simulation becomes more computationally feasible and allows for a systematic investigation of the fundamental heat transfer and fluid dynamics in the integrated toroidal inductor with nanofluid cooling and a microchannel heat sink under the specified conditions.

2.1 Geometrical model

To investigate the cooling of an integrated toroidal octagonal inductor soldered onto a microchannel cooler with fluid flow, the geometry of the modeling domain is illustrated in Figure 1. In Figure 1, a detailed view showcases the deposition of a micro-coil onto a substrate. This entire arrangement is then placed on a heat sink that has been designed with rectangular fins. The substrate is in the shape of a square with dimensions $H \times H \times H_{sub}$.

When electrical current flows through the integrated toroidal micro-coil, the inherent electrical resistances within the circuit give rise to the production of heat through a phenomenon known as Joule heating. As the electrical current becomes more concentrated within a confined space, it leads to an increased current density, further intensifying the generation of heat. Recognizing the need to counterbalance this excess heat, an advanced thermal dissipation system has been employed. Notably, the heat sink is equipped with microchannels through which a cooling fluid circulates. The primary objective of this intricately designed apparatus is to facilitate efficient heat transfer and substantially enhance the cooling process of the integrated toroidal inductor. By leveraging this innovative approach, the detrimental effects of excessive heat generation are effectively mitigated, ensuring the optimal performance and longevity of the system.

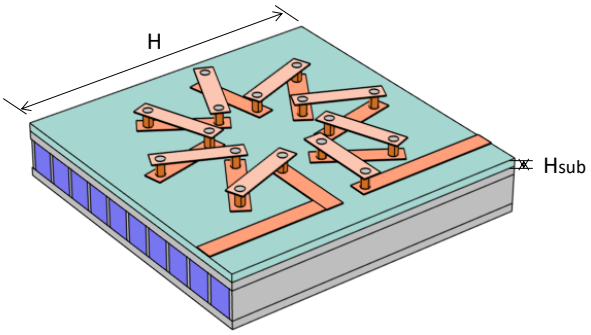

Figure. 1. *Geometry of the modeling domain*

Figure 2 illustrates the geometry of the integrated toroidal octagonal inductor, wherein a micro-coil is positioned atop a substrate. This micro-coil is composed of a superior layer and an inferior layer, interconnected by cylindrical vias. These cylindrical vias assume a critical role in establishing a pathway of low resistance, facilitating the seamless flow of current between the two layers of the integrated inductor. This integration is essential as it empowers the inductor to operate with remarkable efficiency within the intricate spaces of microelectronic circuits or devices for which it is tailored. By effectively promoting current transfer between the layers, this integration significantly contributes to the overall optimal performance and functionality of the system, aligning seamlessly with the specific requirements of its design.

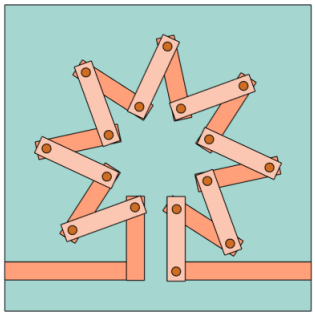

Figure 2. *Geometry of integrated toroidal octagonal inductor*

Figure 3 showcases the geometrical attributes of the micro-coil, which features a toroidal shape. The illustration outlines the Input/Output (I/O) Via points, indicating where the input and output connections are located. The Figure provides a visual representation of the following parameters:
r_{in}: Inner radius of the micro-coil.
r_{out}: Outer radius of the micro-coil.
w: Metal width of the micro-coil.
t: Metal thickness of the micro-coil.
L: Metal length of the micro-coil.

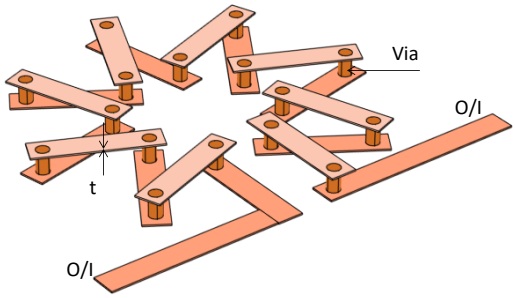

Figure 3. *Geometrical parameters of the octagonal micro-coil*

The intricate dimensions of both the study domain and the micro-coil's geometry are comprehensively illustrated and detailed in Table 1.

Table 1. *Geometrical parameters*

Parameters	**Value**
r_{in} : Inner radius	1800 µm
r_{out}: Outer radius	5200 µm
w : Metal width	600 µm
t : Metal thickness	35 µm
L: Metal length	3400 µm
L_{via}: Via thickness	550 µm
H: Length of substrate	10200 µm
H_{sub}: Depth of substrate	275 µm

The configuration of the heat sink can be adapted to different shapes, including circular, rectangular, or custom designs that are easy to fabricate. However, due to practical fabrication constraints, a rectangular shape is often preferred. Within the heat sink structure, the inclusion of Microchannels is a prominent feature, intended for facilitating fluid flow. These Microchannels predominantly serve as a means for indirect liquid cooling, which is a widely employed technique. As depicted in Figure 4, the heat sink is presented with rectangular fins and microchannels, embodying the specified geometry. The specific design parameters include the

fin count, denoted as N_f=10, and the count of microchannels, denoted as N_{mc}=11. This configuration aims to enhance the heat dissipation efficiency and overall cooling performance of the system. Fluid enters the microchannels with an initial temperature of T_{in}, and exits with a reduced temperature denoted as T_{out}.

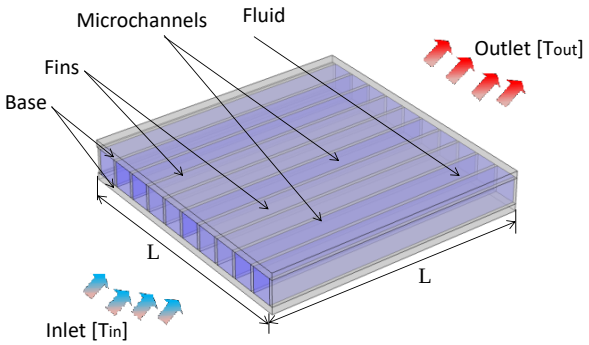

Figure 4. *Heat sink with rectangular fins and microchannels*

The microchannels are characterized by several dimensions: a length denoted as L, a thickness represented as s, the thickness of the fins indicated as a, the height of the microchannels designated as h, and a base thickness of the heat sink denoted as b.

The design parameters of the microchannel heat sink play a crucial role in enhancing heat dissipation efficiency in the system. The use of rectangular fins in the microchannel heat sink is a deliberate design choice. Fins are extended surfaces that increase the heat transfer area, allowing for more efficient dissipation of thermal energy. The rectangular shape provides a balance between structural stability and increased surface area, facilitating optimal heat exchange with the surrounding fluid. The parameter N_f represents the number of fins in the microchannel heat sink. In this case, there are 10 rectangular fins integrated into the heat sink structure. Having multiple fins increases the total surface area available for heat transfer, enabling a higher rate of heat dissipation. The microchannels are passages through which the cooling fluid flows, extracting heat from the integrated inductor. More microchannels provide additional pathways for the fluid to absorb heat, enhancing the overall cooling capacity.

Table 2 illustrates the dimensions of the heat sink with microchannels.

Table 2. *Dimensions of heat sink with microchannels*

Specifications	Value (μm)
Length of microchannels, L	10200
Thickness of microchannels, s	400
Thickness of fins, a	563
Height of microchannels, h	1000
Base thickness, b	275
Number of fins, N_f	10
Number of microchannels, N_{mc}	11

2.2 Governing equations and boundary conditions

In a microchannel heat sink setup, it's typical for the upper wall of the sink to be connected to the lower integrated inductor. The heat transfer process unfolds in two stages: initially, heat travels from the integrated inductor to the microchannels through conduction. To accurately anticipate the thermal and flow behaviors of the integrated inductor, a three-dimensional model that considers both solid and fluid components is utilized. Water with an inlet velocity of u = 0.2 m/s and a temperature of T_{in} = 25°C is used as cooling fluid. This choice of cooling fluid and its specified conditions play a vital role in shaping the heat transfer

characteristics within the system. The properties of the cooling fluid and its interaction with the integrated inductor significantly impact the efficiency of the cooling mechanism and consequently influence the overall performance of the system.

The choice of water as a cooling fluid, along with the specified conditions (inlet velocity u = 0.2 m/s and inlet temperature T_{in} = 25°C), plays a crucial role in shaping heat transfer characteristics and influencing the overall efficiency of the cooling mechanism in the integrated toroidal inductor. Water is known for its relatively high thermal conductivity, making it an effective heat transfer medium. The high thermal conductivity allows for efficient absorption of heat from the toroidal inductor, facilitating effective cooling. Water has a high specific heat capacity, meaning it can absorb and store a significant amount of heat energy per unit mass. This property helps in maintaining stable temperatures within the cooling system and prevents rapid temperature spikes. The specified inlet velocity of 0.2 m/s influences the rate at which water flows through the microchannels. This velocity parameter affects the convective heat transfer coefficient and, consequently, the overall heat dissipation efficiency. The specified inlet temperature of 25°C sets the initial conditions for the cooling fluid. This temperature is crucial for understanding the baseline thermal state of the system and evaluating the cooling effectiveness in relation to the initial conditions.

The governing equations governing the behavior within the channels are as follows, with the Navier-Stokes [17-26] equations stated in the subsequent manner:

$$\nabla \rho_{nf} v = 0 \tag{1}$$

$$\rho_{nf}\left[\frac{\partial v}{\partial t} + v.\nabla v\right] = -\nabla p + \mu_{nf}\nabla^2 v \tag{2}$$

Where:

∇ : gradient operator,

ρ : density of the fluid,

v : velocity vector,

t : time,

p : pressure,

μ : dynamic viscosity,

∇^2 : Laplacian operator.

The equation governing heat transfer is expressed as follows:

$$\rho_i C_{p_i}\left[\frac{\partial T}{\partial t} + v_i.\nabla T\right] = k_i \nabla^2 T + Q \tag{3}$$

Where:

k : thermal conductivity,

T : temperature,

ρ : density of the fluid,

C_p : specific heat capacity,

Q : heat sources in conductor.

Boundary conditions are defined as follows:

At the inlet of microchannels:

$$u = u_0 \tag{4}$$

$$v = w = 0 \tag{5}$$

$$T = T_{in} \tag{6}$$

At the outlet of microchannels:

$$u = v = w = 0 \tag{7}$$

Interface between two different materials:

$$k_1 \frac{\partial T}{\partial \eta}\bigg|_{\text{interface}} = k_2 \frac{\partial T}{\partial \eta}\bigg|_{\text{interface}} \tag{8}$$

$$T_1 = T_2 \tag{9}$$

The average heat transfer coefficient of the microchannel heat sink, given by [27]

$$h_{mchs} = \frac{q_{in}}{\overline{T_w} - T_{in}} \tag{10}$$

$\overline{T_w}$: average temperature of the microchannel wall.

The Reynolds number is defined as [28-34]

$$R_e = \frac{\rho u_{in} D_h}{\mu} \tag{11}$$

μ is the fluid viscosity, D_h (μm) is the hydraulic diameter defined as follows:

$$D_h = \frac{2h_f .s}{h_f + s} \tag{12}$$

The Nusselt number describes the ratio of convective to conductive heat transfer according to

$$Nu = \frac{D_h .h_{mchs}}{k_f} \tag{13}$$

Where k_f is the fluids thermal conductivity.

Total thermal resistance of the heat sink is calculated as [35-42]

$$R = \frac{T_{\max} - T_{in}}{q} \tag{14}$$

$T_{\max}$: maximum heat sink temperature,

q : heat flux on the microchannel wall.

This represents a resistance that includes the caloric resistance of the fluid and conduction resistance through the microchannel base.

The pressure drop through the whole domain (including inlet and outlet extension) is calculated as

$$\Delta P = P_{nf,in} - P_{nf,out} \tag{15}$$

2.3 Nanofluid properties

The thermodynamic characteristics [9, 43-47] of the nanofluid play a significant role in influencing fluid flow and heat transfer dynamics. In this particular investigation, a coolant is employed consisting of CuO nanoparticles suspended in water for one case, while another case employs Al_2O_3 nanoparticles suspended in water as the coolant.

$$\rho_{nf} = (1-\varphi)\rho_f + \varphi\rho_p \tag{16}$$

$$\frac{k_{nf}}{k_f} = \frac{k_p + 2k_f - 2\varphi(k_f - k_p)}{k_p + 2k_f - 2\varphi(k_f - k_p)} \tag{17}$$

$$(\rho C_p)_{nf} = (1-\varphi)(\rho C_p)_f + \varphi(\rho C_p)_p \tag{18}$$

$$\mu_{nf} = \mu_f (1-\varphi)^{-2.5} \tag{19}$$

Where ρ, k, C_p, μ, and φ are the density, conductivity, specific heat capacity, viscosity and solid concentration of nanoparticles, respectively. The subscripts nf, f and p indicate nanofluid, basic fluid, and particles, respectively.

2.4 Mesh of study domain

To ensure both efficient computation and high accuracy, the computational regions encompassing both fluid and solid components are constructed using finely structured mesh cells. The utilization of an unstructured triangular regular mesh has been employed across all domains, facilitating optimal modeling.

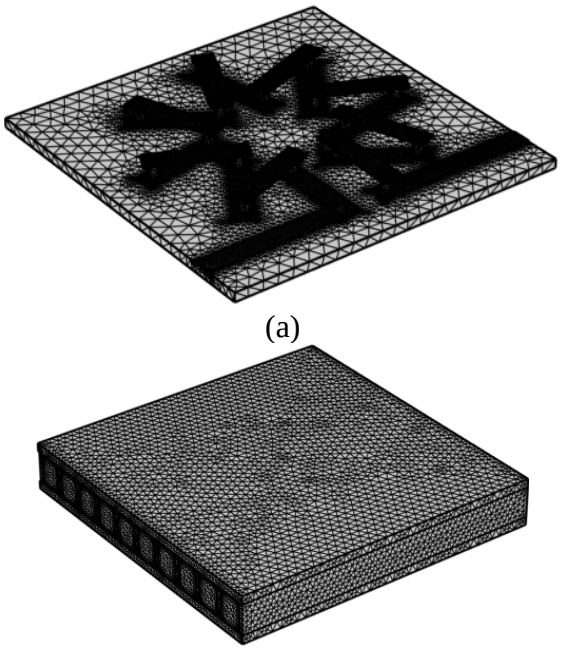

(a) (b)

Figure 5. *Mesh, (a) Study domain with, (b) integrated toroidal inductor with heat sink*

2.5 Physical properties of materials

Table 3 illustrates the thermophysical properties of the materials involved in the setup. The micro coil is crafted from copper, with a Kapton substrate supporting it. The heat sink employed is made of aluminum.

Table 3. *Thermophysial properties of materials*

Material	**Density ($kg\ m^{-3}$)**	**Heat capacity ($J\ kg^{-1}\ K^{-1}$)**	**Thermal conductivity ($W\ m^{-1}\ K^{-1}$)**
Aluminum (Al)	2719	871	202.4
Copper (Cu)	8700	385	400
Kapton	900	710	2000

Table 4 provides an overview of the thermophysical properties of the base fluid and the nanoparticles [48, 49], encompassing key parameters such as density, heat capacity, thermal conductivity, and viscosity. The base fluid utilized in this context is water, while the nanoparticles under consideration include CuO and Al_2O_3.

Table 4. *Thermophysial properties of base fluid and nanoparticles*

Material	**Density (kg^{-3})**	**Heat capacity ($J\ kg^{-1}\ K^{-1}$)**	**Thermal conductivity ($W\ m^{-1}\ K^{-1}$)**	**Viscosity (Pa s)**
Water	997.1	4179	0.613	1.814×10^{-5}
CuO	6500	540	18	-
Al_2O_3	3880	773	40	-

3. Results and discussion

The outcomes of the mathematical model, which intricately combines the Navier-Stokes equations, heat transfer equations, and a set of defined boundary conditions, have been successfully attained through the application of the finite element method. Within the simulation framework, an electrical current intensity of 1.4 A has been integrated as an integral part of the computation procedures. This simulation [50-53] endeavor has yielded invaluable insights into multiple facets of the system under scrutiny, including temperature, velocity, and pressure dynamics. The performance evaluation of the integrated inductor utilizing nanofluids within a microchannel heat sink has been meticulously analyzed. A comparative evaluation involving three distinct fluids is meticulously conducted within this section. The findings are succinctly visualized through graphical representations that depict the relationships among temperature, Reynolds Number, Nusselt Number, and thermal resistance concerning the variable nanofluid volume fraction (φ). Moreover, the study delves into the variation of pressure levels, meticulously illustrating their correlation with the aforementioned nanofluid volume fraction (φ). These findings provide a comprehensive understanding of the dynamic interplay between fluid dynamics, heat transfer, and system behavior in the context of integrated inductor cooling using nanofluids and a microchannel heat sink.

Figure 6 depicts the temperature distribution within the integrated toroidal octagonal inductor when operating without a heat sink. The analysis reveals a maximum temperature of 89.2 °C within the structure. Within the micro-coil itself, the temperature reaches its highest point. As the thermal energy propagates, temperature degradation is observed as it extends to the substrate. Notably, at the upper corner of the substrate, the temperature reaches its minimum value, measuring at 39 °C. This visualization offers valuable insights into the thermal behavior of the system in the absence of a heat sink.

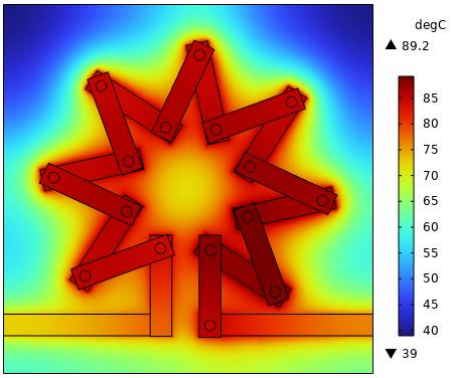

Figure 6. *Temperature distribution in integrated toroidal octagonal inductor without heat sink*

Figure 7 vividly illustrates the distribution of temperature within the integrated toroidal octagonal inductor subsequent to the integration of a heat sink employing pure water cooling. It is noteworthy that the highest temperature recorded within this configuration reaches 70.4 °C, marking a substantial reduction compared to the temperature profile observed in the absence of a heat sink. In the fluid region, the minimum temperature registers at approximately 25 °C, aligning with the initial temperature of the fluid. This transformation in temperature distribution across the integrated inductor serves as compelling evidence of the profound impact instilled by the heat sink, employing pure water cooling as the cooling mechanism.

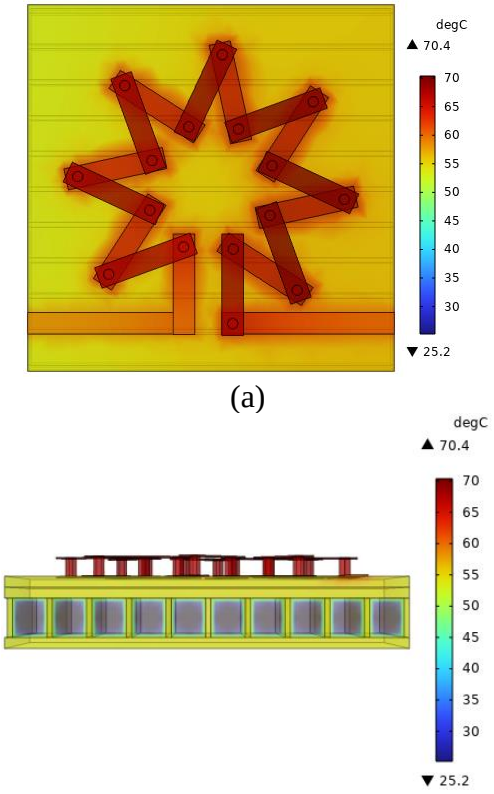

Figure 7. *Temperature distribution in integrated toroidal octagonal inductor with heat sink using pure water cooling, (a) bottom view, (b) front view*

Figure 8 portrays the temperature distribution within the heat sink employing pure water cooling. It is noteworthy that the highest temperature recorded in this configuration reaches 56.2°C. Additionally, the minimum temperature is observed in the input fluid.

The integration of a heat sink, especially with pure water cooling, results in a substantial reduction in the maximum temperature within the integrated toroidal inductor, demonstrating the effectiveness of the cooling system in managing temperatures and enhancing thermal performance.

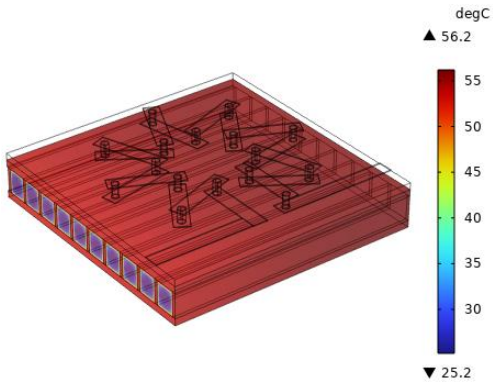

Figure 8. *Temperature distribution in heat sink using with water cooling*

Figure 9 illustrates the temperature distribution within the micro-coil configuration, highlighting the improvements achieved by implementing a pure water cooling mechanism. The visualization emphasizes a maximum temperature of 70.4°C in the upper layers of the configuration. Importantly, the lowest temperature is observed at the input and output of the

inductor, while the lower layers experience temperatures that are notably lower than those present in the upper layers.

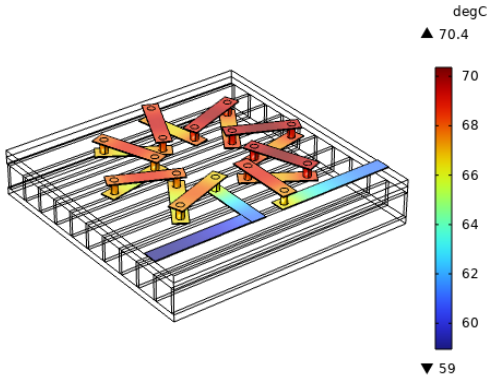

Figure 9. *Temperature distribution in micro-coil using pure water cooling*

Figure 10 portrays the distribution of viscosity within the integrated toroidal octagonal inductor following the incorporation of a heat sink using water cooling integration. The visualization encompasses two perspectives: (a) the global domain and (b) a bottom view. Remarkably, the maximum viscosity observed reaches 0.18 m/s. The depiction of viscosity lines is notably oriented in alignment with the direction of the microchannels. Additionally, arrows are employed to indicate the flow direction, conveying the movement of fluid from the inlet to the outlet. This visualization encapsulates the intricacies of fluid behavior within the system, offering insights into the dynamic viscosity distribution that influences the heat transfer efficiency and overall performance.

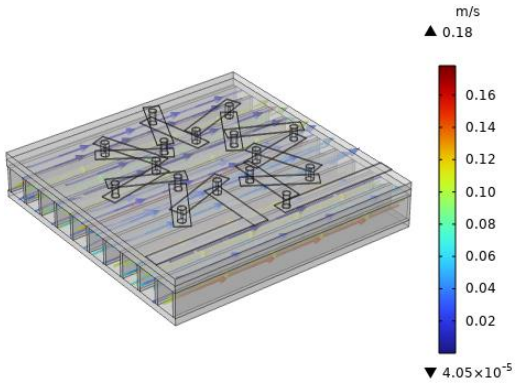

(a)

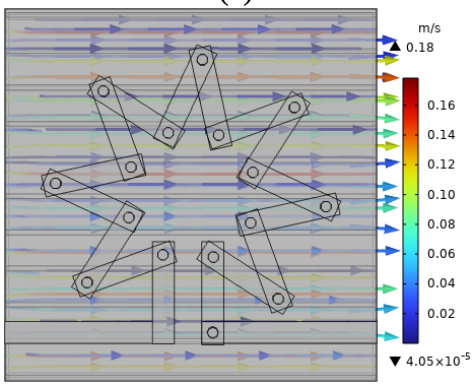

(b)

Figure 10. *Viscosity distribution in integrated toroidal octagonal inductor with heat sink using pure water cooling, (a) global domain, (b) bottom view*

Figure 11 showcases the magnetic velocity profile within the system, depicted from two distinct viewpoints: (a) focusing on the microchannels and (b) featuring a cross-section along the microchannel. Notably, the magnitude of velocity assumes significance at the center of the cross-section along the microchannel, signifying heightened fluid movement at this point. In contrast, the velocity magnitude is comparatively smaller along the microchannel walls. This visual representation provides crucial insights into the magnetic field's influence on fluid motion within the microchannels, delineating areas of intensified and subdued flow for a comprehensive understanding of the system's behavior.

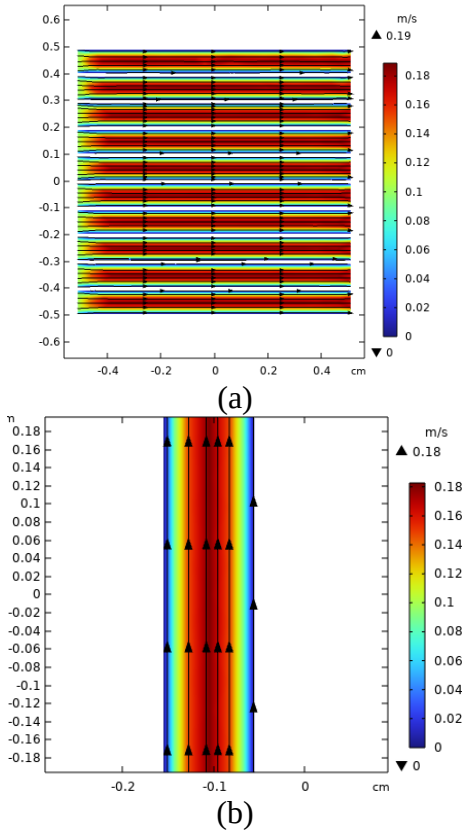

Figure 11. *Velocity magnetic profile, (a) microchannels, (b) cross section along the microchannel*

Figure 12 presents the distribution of pressure within the integrated toroidal octagonal inductor following the integration of a heat sink using water cooling. The visualization captures the maximum pressure, which reaches 31.5 Pa. Particularly noteworthy is the maximum pressure observed at the extremity of the microchannel, specifically at the fluid inlet point. This depiction offers valuable insights into the pressure dynamics that influence fluid behavior and thermal performance within the system, enhancing the understanding of pressure distribution effects under the influence of the heat sink and water cooling mechanism.

Figure 13 depicts the extensive temperature and thermal gradient distribution across the x-y cross section at z=0, subsequent to the integration of a heat sink using water cooling. The visualization showcases a peak temperature of 68.7°C. Notably, the directional arrows indicating the thermal gradient's direction are oriented from the inductor downwards towards the heat sink. This visual representation offers a comprehensive insight into the temperature profile and thermal gradients within the system, elucidating the thermal dynamics and behaviors facilitated by the heat sink utilizing the water cooling mechanism.

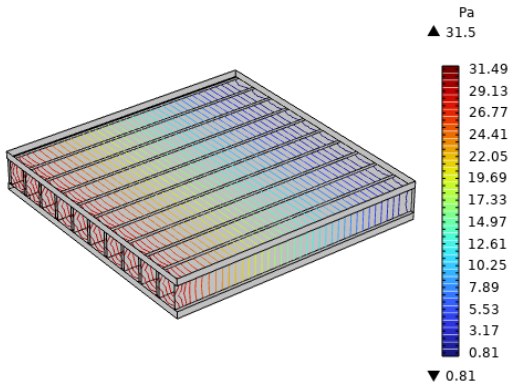

Figure 12. *Pressure distribution in integrated toroidal octagonal inductor with heat sink using water cooling*

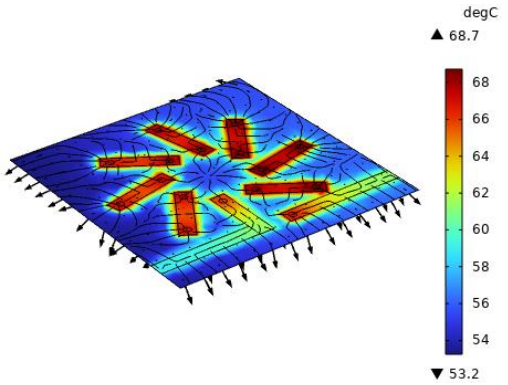

Figure 13. *Distribution of temperature and thermal gradient along the x-y cross section at z=0, with heat sink using water cooling*

In this section, the exploration delves into the impact of nanofluids on heat transfer and laminar flow within the integrated toroidal octagonal inductor. The microchannels are filled with nanofluids, composed of nanoparticles like copper oxide (CuO) or aluminum oxide (Al_2O_3). Two experiments are conducted using nanofluids: water with CuO nanoparticles and water with Al_2O_3 nanoparticles. Both CuO-water and Al_2O_3-water combinations yield nanofluids with enhanced thermal properties and improved heat transfer capabilities compared to pure water. The base of the nanofluid, water, offers excellent heat transfer capacity. CuO and Al_2O_3 nanoparticles act as performance-enhancing agents, elevating the thermal attributes of the nanofluids. These nanoparticles possess unique characteristics that enhance thermal conductivity and heat absorption capacity within the fluid. Importantly, CuO and Al_2O_3 exhibit thermal stability properties, further contributing to the nanofluids' overall performance enhancement.

Figure. 14 presents the impact of nanofluid volume fraction on the temperature distribution within the integrated toroidal octagonal inductor. Simultaneously. The volume fraction is indicated by the fraction factor φ. When the volume fraction is 2%, the use of the nanofluid CuO-water results in a maximum temperature (T_{max}) of 63.5°C within the integrated inductor. In contrast, employing the nanofluid Al_2O_3-water yields a slightly higher T_{max} of 66.7.2°C. Increasing the volume fraction to 4%, the Tmax decreases to 53.3°C with the nanofluid CuO-water and to 54.9°C with the nanofluid Al_2O_3-water. Further elevating the volume fraction to 6%, the Tmax diminishes to 50°C with the nanofluid CuO-water, and to 51°C with the nanofluid Al_2O_3-water.

Figure. 14, depicting the impact of nanofluid volume fraction on temperature distribution, reveal a consistent and noteworthy trend. As the volume fraction of nanofluid increases, the maximum temperature within the integrated inductor decreases. This observation holds true for both CuO-water and Al_2O_3-water nanofluids. The slightly higher T_{max} values for

Al_2O_3-water at each volume fraction suggest that the nanoparticle concentration in nanofluids contributes to enhanced heat dissipation and thermal regulation. This emphasizes the potential of nanofluids with higher fraction factors to achieve lower temperature peaks, a crucial aspect in optimizing the thermal performance of the integrated toroidal inductor.

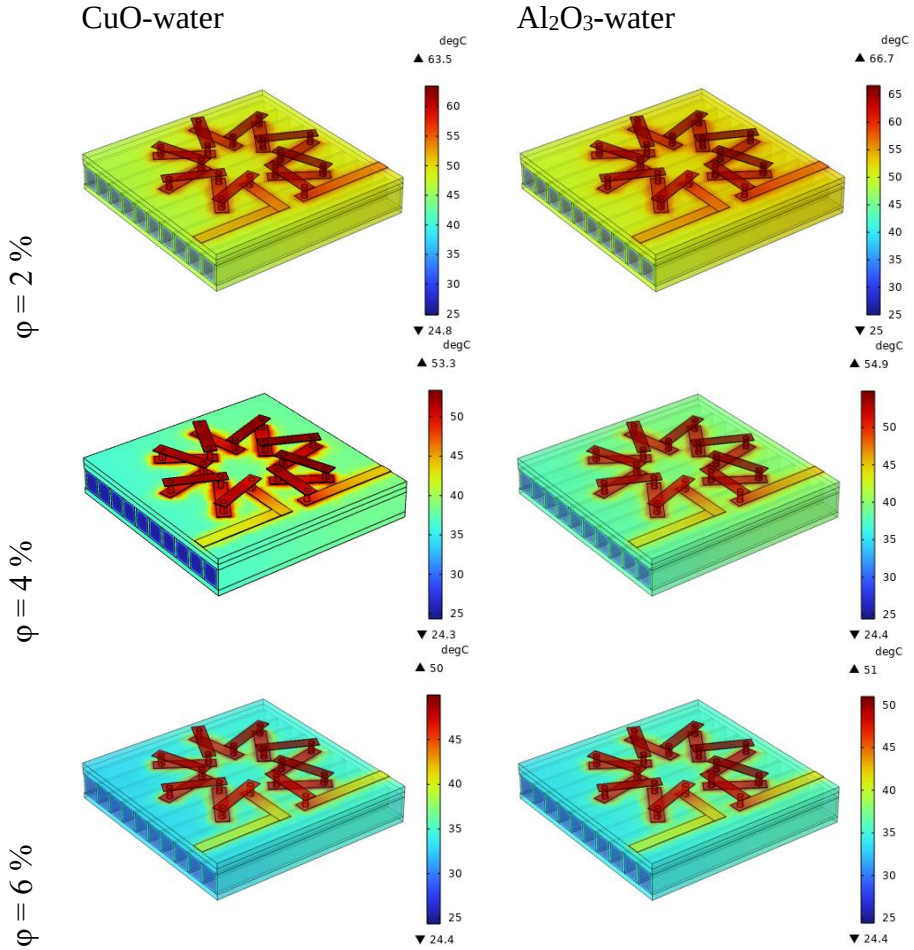

Figure 14. *Effect of nanofluid volume fraction on temperature distribution in integrated toroidal octagonal inductor*

Figure. 15 examines the effect of nanofluid volume fraction on temperature distribution in the heat sink. When the volume fraction is 2%, the use of the nanofluid CuO-water results in a Tmax of 49°C within the integrated inductor. In contrast, employing the nanofluid Al_2O_3-water yields a slightly higher T_{max} of 52.4°C. Increasing the volume fraction to 4%, the T_{max} decreases to 38.5°C with the nanofluid CuO-water and to 40.1°C with the nanofluid Al_2O_3-water. Further elevating the volume fraction to 6%, the T_{max} diminishes to 35°C with the nanofluid CuO-water, and to 36°C with the nanofluid Al_2O_3-water.

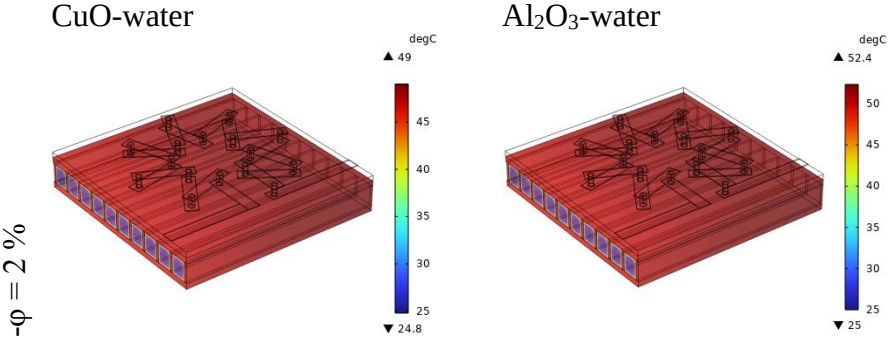

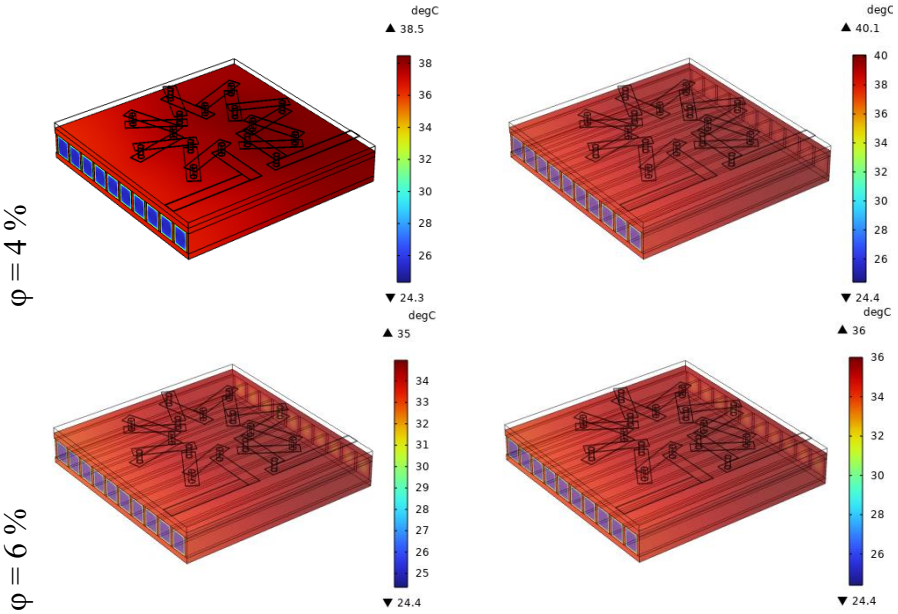

Figure 15. *Effect of nanofluid volume fraction on temperature distribution in heat sink*

Figure. 16 depicts the influence of nanofluid volume fraction on the temperature distribution within the micro-coil. For a φ of 2%, employing the nanofluid CuO-water leads to a maximum temperature of 63.5°C within the micro-coil. Conversely, using the nanofluid Al_2O_3-water results in a slightly higher Tmax of 66.7°C. When the volume fraction is increased to 6%, the Tmax diminishes to 53.3°C with the nanofluid CuO-water, while it reaches 54.9°C with the nanofluid Al_2O_3-water. Further raising the volume fraction to 10%, the Tmax further decreases to 50°C with the nanofluid Cuo-water, and to 51°C with the nanofluid Al_2O_3-water. It is evident that elevating the volume fraction of the nanofluids leads to a reduction in the maximum temperature within the micro-coil. This trend holds true for both nanofluid types, CuO-water and Al_2O_3-water.

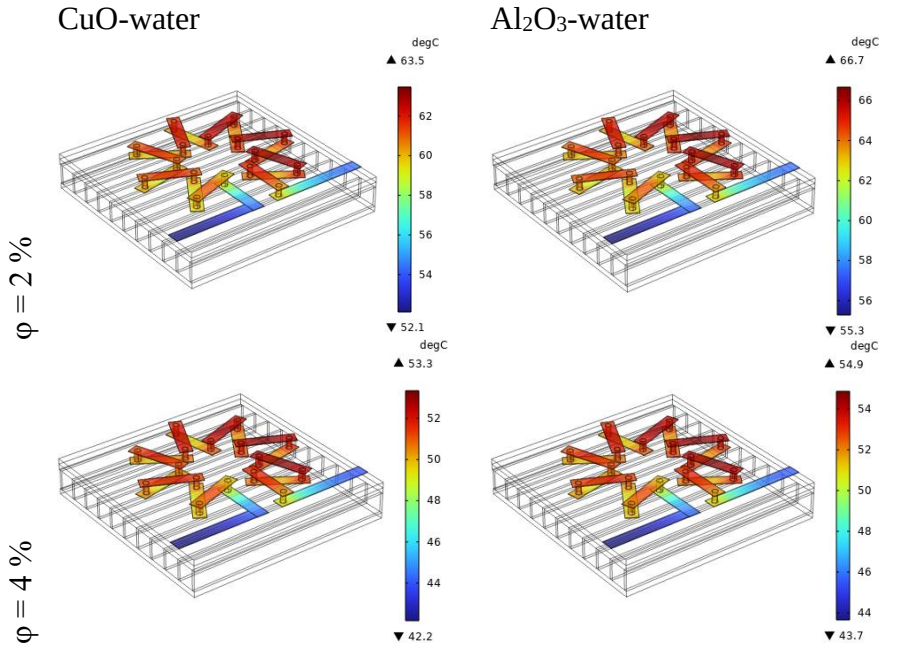

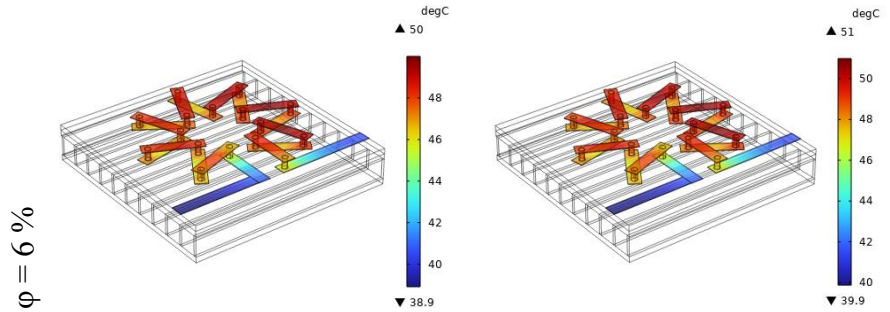

Figure 16. *Effect of nanofluid volume fraction on temperature distribution in micro-coil*

Figure. 17 illustrates the evolution of average temperature concerning nanofluid volume fraction, observed through two distinct perspectives: (a) CuO-water nanofluid and (b) Al_2O_3-water nanofluid. Spanning the range of volume fractions φ at 2%, 4%, 6%, 8%, and 10%, a consistent trend emerges. The average temperature within the micro-coil and heat sink experiences a gradual decrease with increasing nanofluid volume fraction. Notably, when comparing the two types of nanofluids, a consistent pattern is observed: the average temperature achieved with the CuO-water nanofluid remains consistently lower than that with the Al_2O_3-water nanofluid across the entire spectrum of volume fractions.

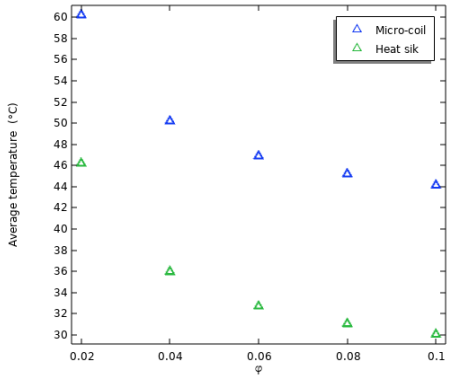

(a)

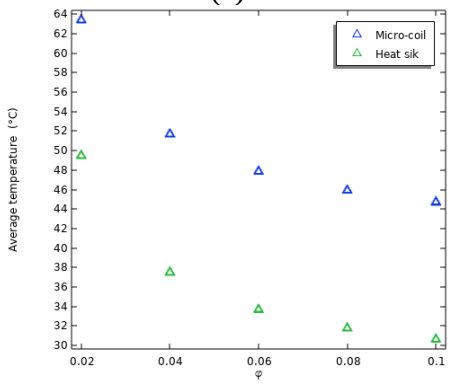

(b)

Figure 17. *Average temperature evolution as function of nanofluid volume fraction φ, (a) Cuo-water, (b) Al_2O_3-water*

Figure. 18 investigates the influence of nanofluid volume fraction on temperature distribution along the midline, focusing on the domain defined by x=0, y=0, and z = -2 103 µm to 550 µm. This analysis is presented through two perspectives: (a) CuO-water nanofluid and (b) Al_2O_3-water nanofluid. As the nanofluid volume fraction (φ) increases, intriguing variations emerge.

Comparing the behavior of the two nanofluid types, a nuanced distinction arises. For the CuO-water nanofluid, as the volume fraction increases, a relatively small variation in temperature is observed along the midline. In contrast, when employing the Al_2O_3-water nanofluid, the temperature remains nearly constant across the range of volume fractions.

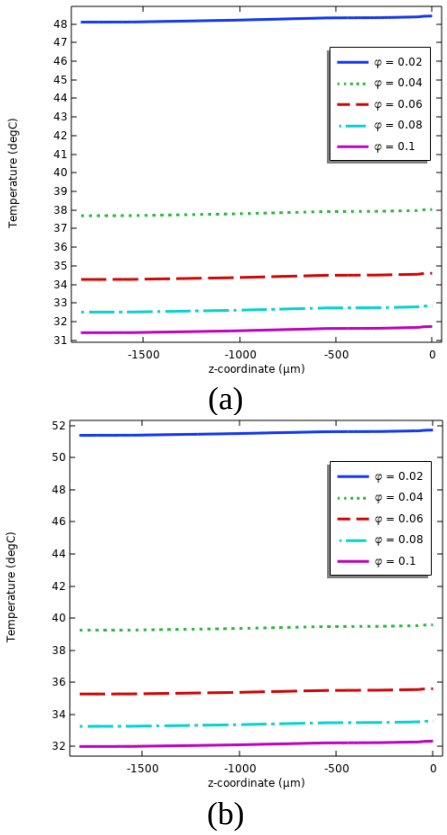

Figure 18. *Effect of nanofluid volume fraction on temperature along the midline x=0, y=0, z= -2 103 µm to 550 µm, (a) Cuo-water, (b) Al_2O_3-water*

Figure 19 elucidates the impact of nanofluid volume fraction on viscosity within the defined study domain. Simultaneously, Figure. 20 provides insight into the effect of nanofluid volume fraction on viscosity from a bottom view. This analysis encompasses two distinct nanofluid compositions: (a) CuO-water nanofluid and (b) Al_2O_3-water nanofluid. Across each nanofluid composition, different volume fractions (φ) of 2%, 4%, and 6% are investigated. Upon considering volume fractions of 2%, 4%, and 6%, both the CuO-water nanofluid and the Al_2O_3-water nanofluid exhibit a maximum viscosity constant of 0.18 m/s. This investigation also reveals a variation in the minimum value of velocity associated with these different volume fractions.

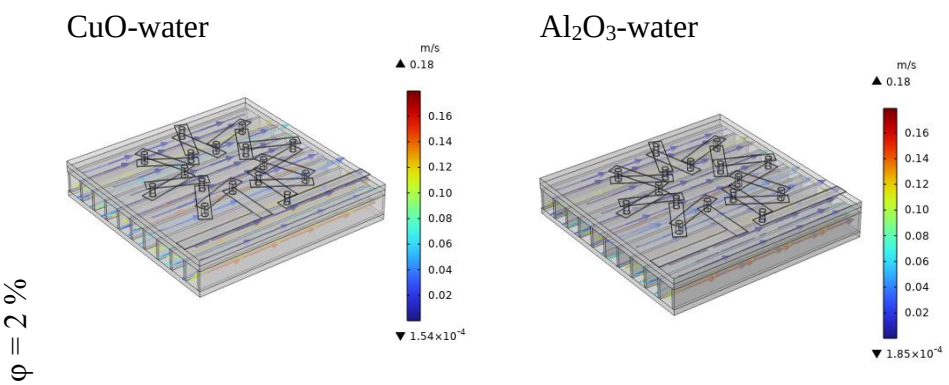

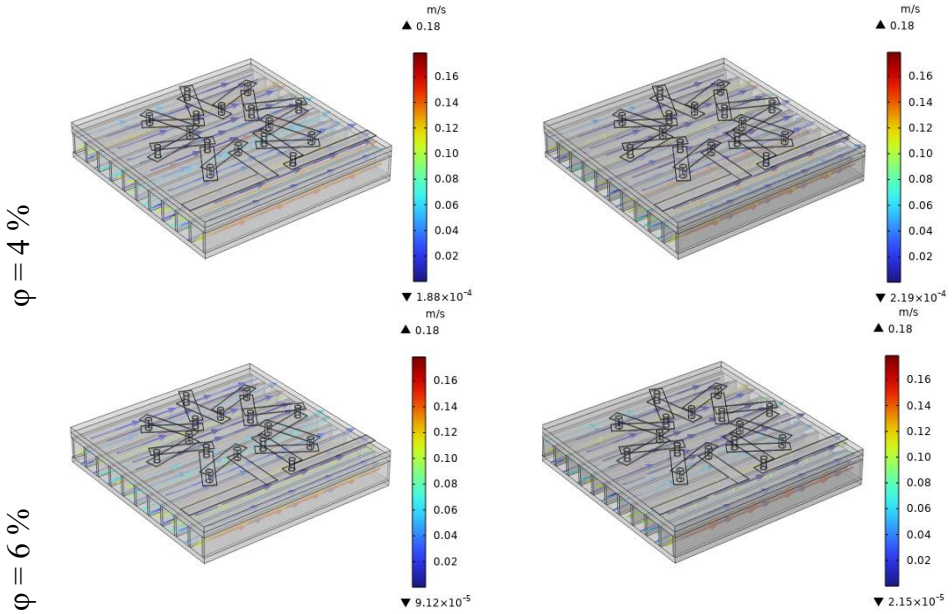

Figure 19. *Effect of nanofluid volume fraction on viscosity in domain study*

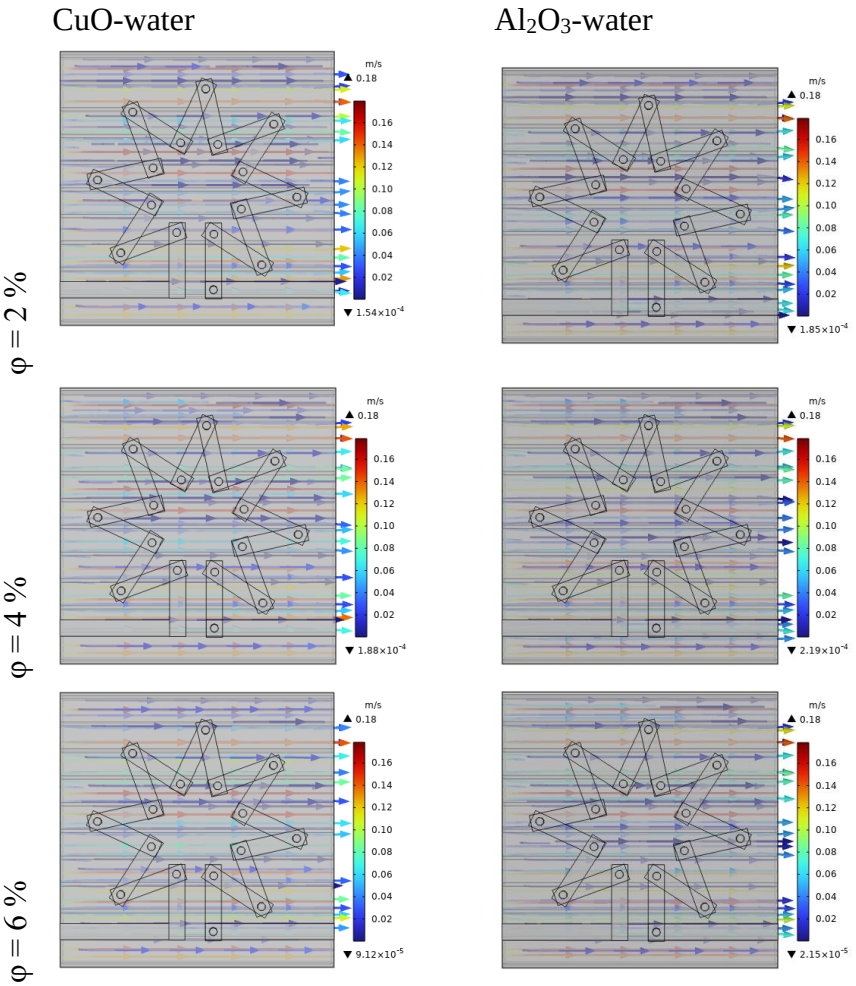

Figure 20. *Effect of nanofluid volume fraction on viscosity in domain study, bottom view*

Figure. 21 illustrates the impact of nanofluid volume fraction on pressure within the study domain. At a φ of 2%, the nanofluid CuO-water exhibits a maximum pressure of 31.6 Pa within the integrated inductor. In contrast, the nanofluid Al_2O_3-water experiences a notably

lower maximum pressure of 31.4 Pa. Transitioning to a φ of 4%, the nanofluid CuO-water displays a maximum pressure of 32.1 Pa, while the nanofluid Al_2O_3-water maintains its previous value of 31.7 Pa. Similarly, at a φ of 6%, the nanofluid CuO-water attains a maximum pressure of 32.7 Pa, while the nanofluid Al_2O_3-water maintains its earlier value of 32 Pa. This comparison indicates a marginal increase in pressure for both nanofluids across the tested volume fractions.

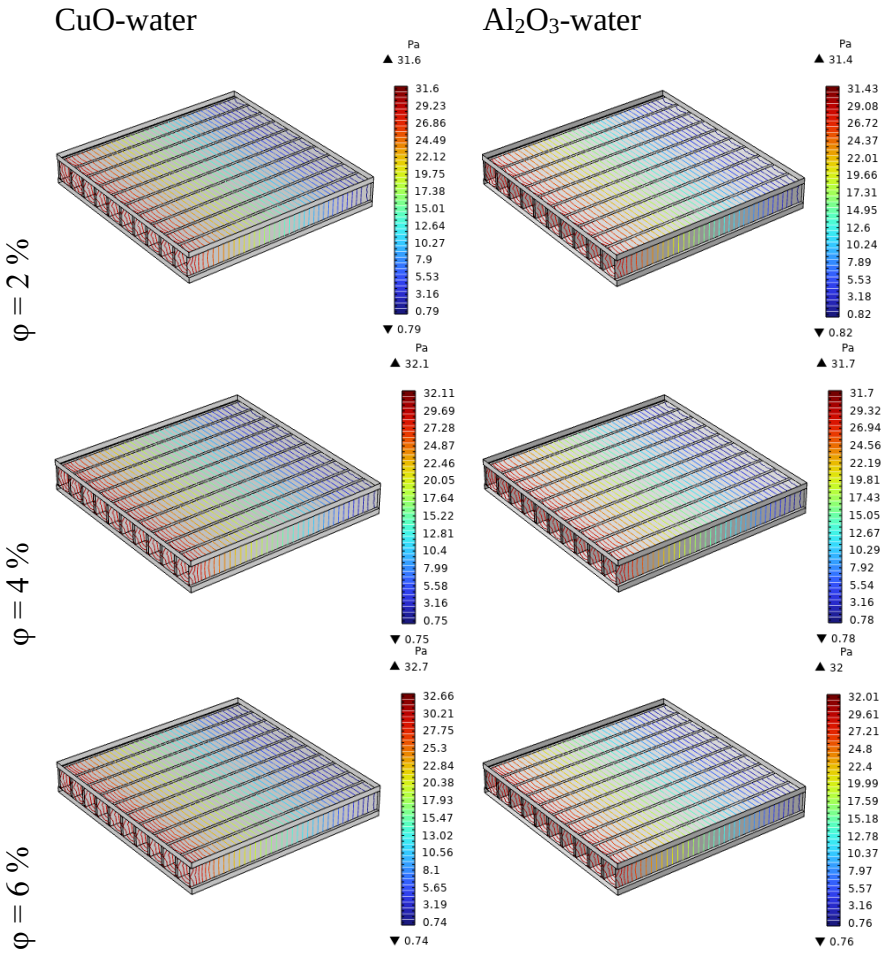

Figure 21. *Effect of nanofluid volume fraction on pressure*

Figure. 22 illustrates the evolution of pressure drop concerning the nanofluid volume fraction. The depicted pressure drop holds paramount importance as a fundamental design parameter, warranting meticulous attention, particularly in the realm of active cooling systems, and even more specifically within microchannel heat sink configurations. Defined as the discrepancy between inlet and outlet pressures, the pressure drop's significance resonates deeply. This parameter's impact is intrinsically tied to the fluidic dynamics within microchannels, a crucial element in achieving optimal cooling outcomes. The pressure drop, at its core, hinges on the dynamic viscosity of the working fluid. The intricate interplay between the fluid's viscosity and the microchannel's geometry defines the pressure drop within the system. Consequently, any shifts in the working fluid provoke corresponding fluctuations in the pressure drop magnitude.

Intriguingly, the investigation unveils a compelling trend with the increase in nanofluid volume fraction (φ). Specifically, both the Al_2O_3-water and CuO-water nanofluid compositions exhibit a discernible uptick in pressure drop magnitude. This insightful revelation emphasizes the profound impact of the choice of working fluid on pressure drop. Notably, when considering

identical flow conditions, opting for Al_2O_3-water nanofluids over CuO-water nanofluids holds the promise of significantly mitigating pressure drop concerns.

Figure. 22 focuses on the evolution of pressure drop with varying nanofluid volume fraction. The discernible increase in pressure drop for both Al_2O_3-water and CuO-water nanofluids highlights the impact of the choice of working fluid on pressure drop. Significantly, the Figure underscores that, under identical flow conditions, opting for Al_2O_3-water nanofluids over CuO-water nanofluids can mitigate pressure drop concerns. This is a crucial insight for the design and optimization of microchannel heat sink configurations, emphasizing the potential advantages of specific nanofluid compositions in reducing pressure drop.

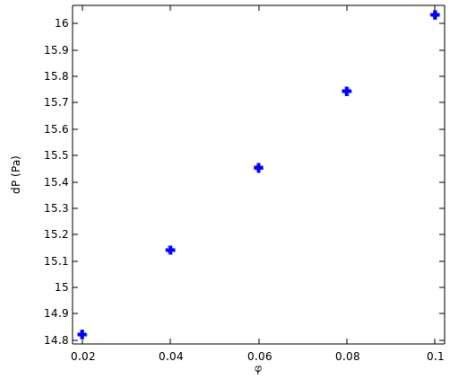

(a)

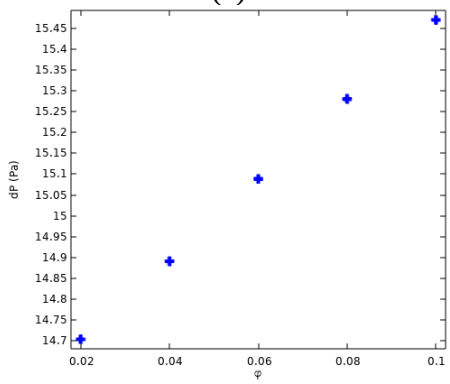

(b)

Figure 22. *Pressure drop evolution as function of nanofluid volume fraction, (a) Cuo-water, (b) Al_2O_3-water*

In Figure. 23, the evolution of the Reynolds number is graphically depicted as a response to changes in nanofluid volume fraction. As the nanofluid volume fraction (φ) escalates, a synchronized elevation in Reynolds number becomes evident for both nanofluid compositions: CuO-water and Al_2O_3-water. This concurrent surge in Reynolds number can be attributed to the amalgamation of metal nanoparticles within the base fluid, concomitant with the amplification of the volume fraction. This dual-factor synergy orchestrates an overall augmentation in Reynolds numbers. The specific ranges of Reynolds numbers further underscore this trend. For CuO-water nanofluid, the Reynolds number spans from 0.45 to 1.85, whereas the analogous range for Al_2O_3-water nanofluid encompasses 0.25 to 1.1. Such delineated ranges provide clear insight into the impact of nanoparticle type and volume fraction on fluid dynamics.

The upswing in Reynolds numbers substantiates an enhanced fluid flow regime attributed to nanoparticle presence and increased volume fraction. The heightened Reynolds numbers signify intensified fluid motion and increased turbulence within the system. It is worth noting that the distinct behaviors exhibited by the two nanofluid compositions, as well as their

disparate Reynolds number ranges, underline the intricate interplay between nanoparticle type, volume fraction, and the resultant fluid flow characteristics. It is also important to consider the influence of density in this context. With a density of 6500 kg/m³ for CuO and 3880 kg/m³ for Al_2O_3, the channel Reynolds number for CuO surpasses that of Al_2O_3 at an identical inlet flow rate. This disparity in density reinforces the nuanced impact of material properties on fluid behavior and highlights the multifaceted nature of fluid dynamics in microchannel heat sinks.

Figure. 23 delves into the evolution of Reynolds number in response to changes in nanofluid volume fraction. The synchronized elevation in Reynolds number with increasing volume fraction for both nanofluid compositions signifies enhanced fluid flow dynamics and increased turbulence within the system. This emphasizes that the presence of metal nanoparticles, coupled with an increase in volume fraction, contributes to intensified fluid motion. The distinct behaviors exhibited by CuO-water and Al2O3-water nanofluids, along with their varying Reynolds number ranges, underscore the intricate interplay between nanoparticle type, volume fraction, and fluid flow characteristics. The Figure provides clear insight into how the choice of nanofluid and its concentration can influence fluid dynamics, a critical consideration in microchannel heat sink design.

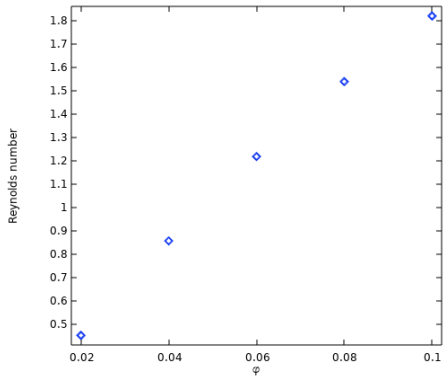

(a)

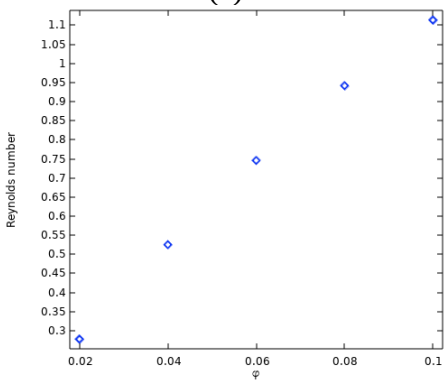

(b)

Figure 23. *Reynolds number evolution as function of nanofluid volume fraction, (a) Cuo-water, (b) Al_2O_3-water*

Figure. 24 displays the evolution of the Nusselt number as a function of nanofluid volume fraction. As φ increases, exhibit an increase in the Nusselt number. The higher Nusselt numbers indicate improved heat exchange between the fluid and surrounding surfaces, reflecting the intensified convective heat transfer within the system. The distinctive behavior exhibited by the two nanofluid compositions, along with their respective Nusselt number ranges, highlights the intricate interplay between nanoparticle type, volume fraction, and convective heat transfer characteristics.

Increasing nanoparticle concentration (φ) has a significant impact on convective heat transfer in toroidal inductor microchannels, contributing to enhanced thermal performance with

CuO-water and Al_2O_3-water nanofluids. As nanoparticle concentration increases, the Nusselt number, which characterizes the convective heat transfer effectiveness, also increases. The Nusselt number is a dimensionless parameter used to quantify the convective heat transfer rate, and its elevation indicates improved heat transfer performance. The Reynolds number, which accounts for the flow regime within the microchannels, may be affected by changes in nanoparticle concentration. The interplay between Reynolds number and Nusselt number is crucial for understanding the convective heat transfer dynamics.

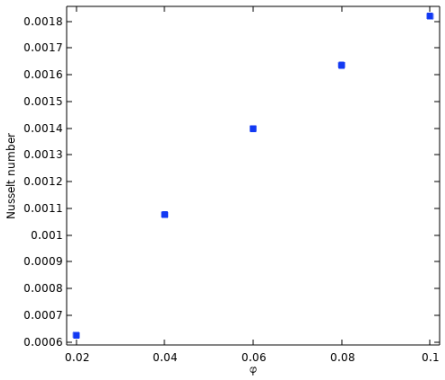

(a)

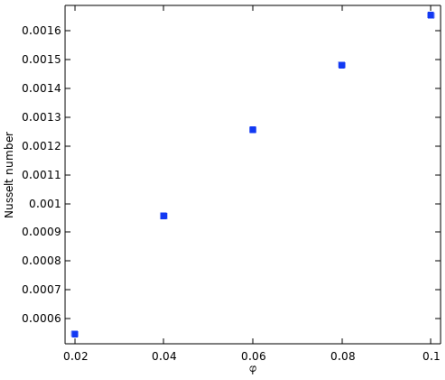

(b)

Figure 24. *Nusselt number evolution as function of nanofluid volume fraction, (a) Cuo-water, (b) Al_2O_3-water*

Figure 25 provides valuable insights into the effectiveness of CuO-water and Al_2O_3-water nanofluids in improving heat transfer within the microchannel heat sink configuration by illustrating the variation in thermal resistance with changes in nanofluid volume fraction. As the volume fraction of the nanofluid increases, there is a noticeable decrease in thermal resistance. This trend is consistent for both nanofluid compositions, CuO-water, and Al_2O_3-water. The lower thermal resistance is attributed to the specific characteristics of the nanofluid compositions. Particularly, the CuO/metal liquid model, featuring CuO with relatively lower thermal conductivity, exhibits the lowest thermal resistance among the tested configurations. The thermal resistance considered here encompasses the caloric resistance of the fluid and the conduction resistance through the microchannel base. Therefore, the observed decrease in thermal resistance with increasing nanofluid volume fraction indicates improved heat transfer efficiency in the microchannel heat sink, emphasizing the positive impact of nanofluids on the cooling system's performance.

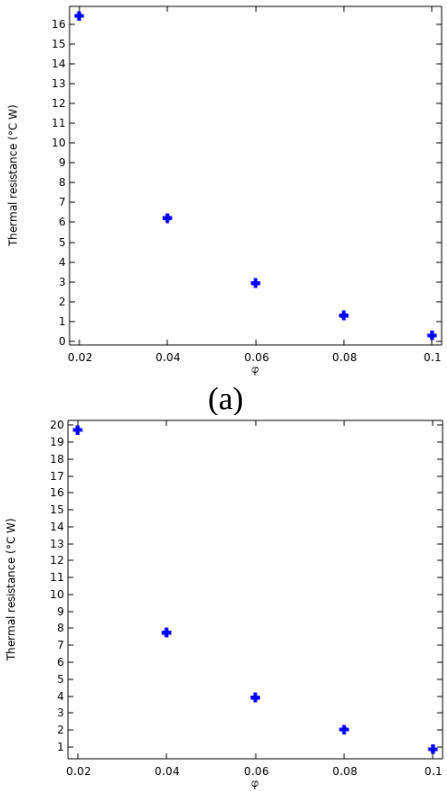

(a)

(b)

Figure 25. *Thermal resistance evolution as function of nanofluid volume fraction, (a) Cuo-water, (b) Al_2O_3-water*

4. Conclusion

The objectives of the study, which included a comprehensive analysis using COMSOL Multiphysics 6.0 3D Computational Fluid Dynamics (CFD), were successful in providing valuable insights into the cooling behavior of the integrated toroidal inductor with nanofluids in microchannels. The study addressed the thermal management challenges associated with integrated inductors, particularly the toroidal octagonal inductor, and explored the effectiveness of nanofluids and a microchannel heat sink in enhancing heat dissipation. This mathematical model combines the Navier-Stokes equations of fluid dynamics with the heat transfer equations. To achieve this goal, an overview of the geometry of the entire cooling system is provided, the configuration of the integrated inductor with heat sink is described in detail, and the microchannels for nanofluid circulation are represented. In this simulation, variables such as temperature, velocity, pressure, Reynolds number, Nusselt number were studied. When considering the simulated area without heat sinks, a maximum temperature of 89.2 °C was observed. Replacing water as coolant in the microchannel heat sink resulted in a maximum temperature of 70.4 °C in the studied range, along with a maximum viscosity of 0.18 m/s. The recorded peak pressure reached 31.5 Pa. Furthermore, the maximum temperature inside the regenerator was found to be 56.2°C. Additionally, the analysis addresses the effect of nanofluids containing CuO and Al_2O_3 nanoparticles. As the nanofluid volume fraction increases, a continuous decrease in the overall temperature within the integrated inductor is observed. This trend applies to two types of nanofluids: CuO-water and Al_2O_3-water. Interestingly, higher nanofluid concentrations, especially Al_2O_3-water, showed a slight increase in T_{max} values compared to CuO-water at each volume fraction. As the volume fraction of the nanofluid increases, the average temperature within the integrated inductor and heat sink decrease. The viscosity remained relatively stable despite fluctuations in volume fraction, suggesting that other factors may play a more important role in influencing fluid viscosity, such as the type and

concentration of nanoparticles or the interaction between the nanoparticles and the base fluid. Furthermore, the increase in nanofluid volume fraction was found to elevate Reynolds number, and Nusselt number. Conversely, the increase in nanofluid volume fraction was found to lead to a decrease in thermal resistance. This observation underscores the potential benefits of using CuO-based nanofluids in terms of enhancing heat transfer efficiency and reducing thermal resistance, which are crucial aspects in optimizing cooling mechanisms for integrated systems. In conclusion, the incorporation of nanofluids, containing CuO and Al_2O_3 nanoparticles, demonstrated enhanced heat transfer performance within the integrated inductor, with the nanofluid volume fraction influencing various parameters related to fluid flow and heat transfer.

The trends indicate that increasing nanofluid volume fraction generally leads to improved heat transfer characteristics in the integrated toroidal inductor. These improvements are observed in reduced temperatures, increased pressure drop, altered viscosity, higher Reynolds and Nusselt numbers, and decreased thermal resistance. The choice of nanofluid composition and its volume fraction plays a crucial role in influencing these parameters and enhancing the overall thermal performance of the cooling system.

References

1. Tuckerman, D.B. and R.F.W. Pease, *High-performance heat sinking for VLSI.* IEEE Electron device letters, 1981. **2**(5): p. 126-129.
2. Harley, J.C., et al., *Gas flow in micro-channels.* Journal of fluid mechanics, 1995. **284**: p. 257-274.
3. Lee, P.-S. and S.V. Garimella, *Thermally developing flow and heat transfer in rectangular microchannels of different aspect ratios.* International journal of heat and mass transfer, 2006. **49**(17-18): p. 3060-3067.
4. Natrajan, V. and K. Christensen, *Non-intrusive measurements of convective heat transfer in smooth-and rough-wall microchannels: laminar flow.* Experiments in Fluids, 2010. **49**: p. 1021-1037.
5. Heris, S.Z., S.G. Etemad, and M.N. Esfahany, *Experimental investigation of oxide nanofluids laminar flow convective heat transfer.* International communications in heat and mass transfer, 2006. **33**(4): p. 529-535.
6. Li, C.H. and G. Peterson, *Experimental investigation of temperature and volume fraction variations on the effective thermal conductivity of nanoparticle suspensions (nanofluids).* journal of applied physics, 2006. **99**(8).
7. Mirzaei, M. and M. Dehghan, *Investigation of flow and heat transfer of nanofluid in microchannel with variable property approach.* Heat and Mass Transfer, 2013. **49**: p. 1803-1811.
8. Khoshvaght-Aliabadi, M., *Influence of different design parameters and Al2O3-water nanofluid flow on heat transfer and flow characteristics of sinusoidal-corrugated channels.* Energy conversion and management, 2014. **88**: p. 96-105.
9. Pourfattah, F., et al., *On the thermal characteristics of a manifold microchannel heat sink subjected to nanofluid using two-phase flow simulation.* International Journal of Heat and Mass Transfer, 2019. **143**: p. 118518.
10. Van Erp, R., et al., *Co-designing electronics with microfluidics for more sustainable cooling.* Nature, 2020. **585**(7824): p. 211-216.
11. Cheng, J., et al., *Multi-objective optimization of manifold microchannel heat sink with corrugated bottom impacted by nanofluid jet.* International Journal of Heat and Mass Transfer, 2023. **201**: p. 123634.
12. Frommberger, M., et al., *Integration of crossed anisotropy magnetic core into toroidal thin-film inductors.* IEEE Transactions on microwave theory and techniques, 2005. **53**(6): p. 2096-2100.

13. Kovačević, I.F., A.M. Müsing, and J.W. Kolar, *An extension of PEEC method for magnetic materials modeling in frequency domain.* IEEE transactions on magnetics, 2010. **47**(5): p. 910-913.
14. Lopez-Villegas, J.M., N. Vidal, and J.A. del Alamo. *Toroidal versus spiral inductors in multilayered technologies*. in *2016 IEEE Radio Frequency Integrated Circuits Symposium (RFIC)*. 2016. IEEE.
15. Feng, H., Y. Liu, and J. He. *Broadband PEEC Model Study on Ferrite-core Inductive Devices of Switched Mode Power Supply*. in *2020 6th Global Electromagnetic Compatibility Conference (GEMCCON)*. 2020. IEEE.
16. Sun, H., et al., *Design and Optimization of Multimodule IPPS System With Toroidal Structure.* IEEE Transactions on Plasma Science, 2023. **51**(1): p. 227-233.
17. Pan, Y.-H., et al., *Numerical study on heat transfer characteristics of a pin–fin staggered manifold microchannel heat sink.* Applied Thermal Engineering, 2023. **219**: p. 119436.
18. Sun, S., P. Liebersbach, and X. Qian, *3D topology optimization of heat sinks for liquid cooling.* Applied Thermal Engineering, 2020. **178**: p. 115540.
19. Zhang, H., et al., *Numerical study on the pulsating effect on heat transfer performance of pseudo-plastic fluid flow in a manifold microchannel heat sink.* Applied Thermal Engineering, 2018. **129**: p. 1092-1105.
20. Li, S.-N., et al., *Numerical study on the heat transfer performance of non-Newtonian fluid flow in a manifold microchannel heat sink.* Applied Thermal Engineering, 2017. **115**: p. 1213-1225.
21. Jang, S.P., S.J. Kim, and K.W. Paik, *Experimental investigation of thermal characteristics for a microchannel heat sink subject to an impinging jet, using a micro-thermal sensor array.* Sensors and Actuators A: Physical, 2003. **105**(2): p. 211-224.
22. Zhou, J., et al., *Flow thermohydraulic characterization of hierarchical-manifold microchannel heat sink with uniform flow distribution.* Applied Thermal Engineering, 2021. **198**: p. 117510.
23. Chen, B., et al., *Hydrodynamic and thermal performance of in-line strip-fin manifold microchannel heat sink.* International Journal of Heat and Mass Transfer, 2023. **209**: p. 124131.
24. Luo, Y., et al., *Analysis of thermal performance and pressure loss of subcooled flow boiling in manifold microchannel heat sink.* International Journal of Heat and Mass Transfer, 2020. **162**: p. 120362.
25. Li, Y., et al., *Characteristics of laminar flow and heat transfer in microchannel heat sink with triangular cavities and rectangular ribs.* International Journal of Heat and Mass Transfer, 2016. **98**: p. 17-28.
26. Qu, W. and I. Mudawar, *Analysis of three-dimensional heat transfer in micro-channel heat sinks.* International Journal of heat and mass transfer, 2002. **45**(19): p. 3973-3985.
27. Ghani, I.A., N. Kamaruzaman, and N.A.C. Sidik, *Heat transfer augmentation in a microchannel heat sink with sinusoidal cavities and rectangular ribs.* International Journal of Heat and Mass Transfer, 2017. **108**: p. 1969-1981.
28. Kong, D., et al., *An additively manufactured manifold-microchannel heat sink for high-heat flux cooling.* International Journal of Mechanical Sciences, 2023. **248**: p. 108228.
29. Zhang, J., et al., *Numerical investigation of novel manifold microchannel heat sinks with countercurrent regions.* International Journal of Heat and Mass Transfer, 2023. **214**: p. 124389.
30. Wang, Z., et al., *Sobol sensitivity analysis and multi-objective optimization of manifold microchannel heat sink considering entropy generation minimization.* International Journal of Heat and Mass Transfer, 2023. **208**: p. 124046.

31. Shanmugam, M. and L.S. Maganti, *Multi-objective optimization of parallel microchannel heat sink with inlet/outlet U, I, Z type manifold configuration by RSM and NSGA-II.* International Journal of Heat and Mass Transfer, 2023. **201**: p. 123641.
32. Gilmore, N., V. Timchenko, and C. Menictas, *Manifold microchannel heat sink topology optimisation.* International Journal of Heat and Mass Transfer, 2021. **170**: p. 121025.
33. Yang, M., et al., *Experimental study on single-phase hybrid microchannel cooling using HFE-7100 for liquid-cooled chips.* International Journal of Heat and Mass Transfer, 2020. **160**: p. 120230.
34. Collins, I.L., et al., *A permeable-membrane microchannel heat sink made by additive manufacturing.* International Journal of Heat and Mass Transfer, 2019. **131**: p. 1174-1183.
35. Tang, K., et al., *Thermal-hydraulic Performance of Ammonia in Manifold Microchannel Heat Sink.* Applied Thermal Engineering, 2023: p. 121000.
36. Chen, C., et al., *Design, integration and performance analysis of a lid-integral microchannel cooling module for high-power chip.* Applied Thermal Engineering, 2021. **198**: p. 117457.
37. Yang, M. and B.-Y. Cao, *Numerical study on flow and heat transfer of a hybrid microchannel cooling scheme using manifold arrangement and secondary channels.* Applied Thermal Engineering, 2019. **159**: p. 113896.
38. Yue, Y., S.K. Mohammadian, and Y. Zhang, *Analysis of performances of a manifold microchannel heat sink with nanofluids.* International Journal of Thermal Sciences, 2015. **89**: p. 305-313.
39. Tang, W., et al., *Thermal management of GaN HEMT devices using subcooled flow boiling in an embedded manifold microchannel heat sink.* Applied Thermal Engineering, 2023. **225**: p. 120174.
40. Tang, K., et al., *Simulation and optimization of thermal performance in diverging/converging manifold microchannel heat sink.* International Journal of Heat and Mass Transfer, 2023. **200**: p. 123495.
41. Sarangi, S., et al., *Manifold microchannel heat sink design using optimization under uncertainty.* International Journal of Heat and Mass Transfer, 2014. **69**: p. 92-105.
42. Park, H.S. and J. Punch, *Friction factor and heat transfer in multiple microchannels with uniform flow distribution.* International Journal of Heat and Mass Transfer, 2008. **51**(17-18): p. 4535-4543.
43. Pan, Y., et al., *Study on the flow and heat transfer characteristics of pin-fin manifold microchannel heat sink.* International Journal of Heat and Mass Transfer, 2022. **183**: p. 122052.
44. Lin, Y., et al., *Single-phase and two-phase flow and heat transfer in microchannel heat sink with various manifold arrangements.* International Journal of Heat and Mass Transfer, 2021. **171**: p. 121118.
45. Luo, Y., et al., *A numerical study of subcooled flow boiling in a manifold microchannel heat sink with varying inlet-to-outlet width ratio.* International Journal of Heat and Mass Transfer, 2019. **139**: p. 554-563.
46. Bakhirathan, A., R. Giridhar, and G.K.K. Lachireddi, *Heat Transfer Enhancement for On-Chip Cooling Application Using Novel Composite Heat Sink—Comparative Numerical Study.* IEEE Transactions on Components, Packaging and Manufacturing Technology, 2021. **11**(8): p. 1197-1205.
47. Faraji, H., M. Faraji, and M. El Alami. *Numerical Investigation of the Latent Heat Storage During the Melting Driven Natural Convection Around Heat Source Embedded in a Rectangular Cavity: Application to the Passive Cooling*. in *2018 6th International Renewable and Sustainable Energy Conference (IRSEC)*. 2018. IEEE.

48. Okasha, A.T., et al., *Numerical Study of Single-Layer and Stacked Minichannel-Based Heat Sinks Using Different Truncating Ratios for Cooling High Concentration Photovoltaic Systems.* Sustainability, 2022. **14**(9): p. 5352.
49. Martínez-Maradiaga, D., et al., *Design and testing of topology optimized heat sinks for a tablet.* International Journal of Heat and Mass Transfer, 2019. **142**: p. 118429.
50. Kharbouch, H., et al., *Design and implementation of inductors with variable conductor width integrated in a boost micro converter.* Transactions on Electrical and Electronic Materials, 2021. **22**: p. 519-530.
51. Derkaoui, M., et al., *Design and modeling of octagonal planar inductor and transformer in monolithic technology for RF systems.* Journal of Electrical Engineering & Technology, 2021. **16**(3): p. 1481-1493.
52. Benhadda, Y., et al., *Design for Integrated Planar Spiral Inductor for MEMS.* Periodica Polytechnica Electrical Engineering and Computer Science, 2023.
53. Derkaoui, M., et al., *On-Chip GaN Planar Transformer Design for Highly Integrated RF Systems.* Journal of Circuits, Systems and Computers, 2023. **32**(09): p. 2350149.